

Importance of bond exchange in MnC structural stability and half-metallic ferromagnetism: a comprehensive density functional benchmark study

Abdesalem Houari^{1,*} and Peter E. Blöchl²

¹*Theoretical Physics Laboratory, Department of Physics, University of Bejaia, Bejaia, Algeria*

²*Clausthal University of Technology, Institute for Theoretical Physics,
Leibnizstr.10, D-38678 Clausthal-Zellerfeld, Germany*

(Dated: April 1, 2025)

Recently, a first successful synthesis of the unknown bulk manganese monocarbide (MnC) has been reported. Suggested as a potential superhard material, the compound is found to crystallize in the zincblende (B3) structure. In the present work, we report an exhaustive density functional investigation on structural, electronic and magnetic properties of MnC, using different levels of exchange-correlation approximations. We show that SCAN meta-GGA and PBE0r hybrid functional outperform GGA-PBEsol, HSE06 hybrid functional and the mean field DFT+ $U+V$; in predicting correctly the experimental zincblende structure as the groundstate one. It is demonstrated that the bond exchange plays a crucial role in this stabilization. At theoretical equilibrium, hybrid functionals (PBE0r and HSE06) lead to a metallic behavior of MnC. Semilocal ones (PBEsol and SCAN) and mean field DFT+ $U+V$, however, predict two opposite kinds of half-metallic ferromagnetism; opening a debate on the origin and the nature this behavior. If the latter is confirmed experimentally, MnC could be for importance as a spintronic material.

PACS numbers: 71.10.-w, 71.15.Mb, 71.15.Nc

I. INTRODUCTION

The stoichiometric binary monocompounds arising from late $3d$ transition metal (Mn, Fe, Co, Ni and Cu) and light elements (C, N and O) show a variety of interesting features. First, the monoxides (such as MnO, FeO etc.), are well known since a long time and their properties are well established experimentally and theoretically¹⁻⁴. Adopting all a rocksalt type crystal structure, they have been hugely investigated; especially as a paradigm for the study of strong correlations^{5,6}.

In the case of mononitrides, however, some of them have remained challenging experimentally, until the end of the past century⁷⁻¹⁰. The experimentally observed antiferromagnetic MnN, in distorted rocksalt structure, has been reproduced correctly by means of first principles calculations^{11,12}. On the other side, the crystal structure FeN and CoN was the subject of some debates^{13,14}, but it has been confirmed later that both adopt a zincblende one¹⁵. Finally, NiN and CuN are still not yet synthesized. While they have been the subject of some *ab-initio* calculations¹⁶⁻¹⁸, a disagreement still exists on their ground-state structure.

The situation seems more severe with monocarbides (MnC, FeC etc.) which are hardly known. The difficulty to synthesize these compounds is mainly explained in terms of increased filling of the antibonding states across the late $3d$ series, rendering these monocarbides highly unstable¹⁹⁻²¹. Nevertheless, some theoretical works have been reported in literature. Two investigations on the full series of $3d$ transition metal monocarbides, have been reported^{22,23}. Recently, Szymanski *et al.*²³ have carried out an exhaustive *ab-initio* study on their thermodynamical stability, but only in the rocksalt structure. They found that MnC and FeC are unstable at ambient condi-

tions, because of the metal-metal dimerization; but they could be stabilized at high pressure (and/or temperature). Furthermore, their electron-phonon calculations predicted an unconventional superconductivity in MnC. On the other hand, the authors concluded that the instabilities found in CoC, NiC and CuC cannot be overcome by extrinsic conditions; due to the exceptionally weak metal-carbon bond. In terms of dynamical and mechanical stability, a similar systematic investigation²⁴ has demonstrated that Mn, Fe, Co and Ni monocarbides would prefer a ground-state zincblende structure, rather than a rocksalt one.

The formation enthalpies of the manganese-carbon system have been calculated, showing that the MnC (monocarbide) formation is highly unfavorable²⁵. Recently, however, an experimental investigation has reported its first synthesis (using high-pressure and high-temperature conditions)²⁶. It was found that MnC crystallizes in the fourfold coordinated zincblende (ZB) structure, with a lattice constant of 4.429Å. The performed first-principles calculations have revealed the metallic nature of the compound. According to the authors, the estimated hardness and elastic constants make MnC a potential superhard material. However, no data have been provided about its magnetic properties. On the other side, some previous theoretical studies^{27,28} have pointed out that the zincblende MnC would be a ferromagnetic half-metal. Moreover, an unusual half-metallic ferromagnetism has been described, consisting on a coexistence of localized and itinerant spin moments²⁹. As it is well known, this kind of materials with a full spin polarization (100%) at the Fermi level, are very promising for spintronic applications^{30,31}.

The present work focuses on the ground-state crystal structure, the magnetic ordering and the electronic prop-

erties of MnC. To this end, we carry out first-principles calculations based on density functional theory (DFT); where the exchange-correlation effects are initially accounted for within the generalized-gradient approximation (GGA). Then, we use the current state-of-the-art of density functional based frameworks, as constructed through meta-GGA, range-separated hybrid functionals and the mean-field DFT+ U + V methods.

The paper is organized as follows. We first review the theoretical methods in Sec. II, where the basics of meta-GGA functionals and hybrid DFT are presented; with an emphasis on the HSE06 and the PBE0r functionals. Then, the DFT+ U and its recent extension DFT+ U + V approaches are summarized; with a brief explanation on the *ab-initio* calculation of the onsite U and the intersite V Hubbard parameters. After giving the computational details in Sec. III, we present and discuss the obtained results on the structural stability and the magnetic ordering in Sec. IV. Next, a detailed description and analysis of the electronic structure and chemical bonding (through the electronic densities of states) are presented in Sec. V. Finally, we conclude our investigation, by summarizing the important results, in Sec. VI.

II. THEORY

Eventhough DFT is in principle an exact theory, the exchange-correlation energy functional E_{xc} still remains unknown³². Thus, the practical usage of the Kohn-Sham framework³³ relies entirely on finding suitable approximations to this functional. A panoply of schemes and parameterizations have been invented over time. The main different levels of theoretical advances and approximations are nicely illustrated by the Perdew Jacob's ladder³⁴ of the E_{xc} functionals.

A. meta-GGA

At the third rung of the Perdew Jacob's ladder, one can find the so-called meta generalized gradient approximation (meta-GGA). In fact, it is the highest level of the hierarchy avoiding the full non-locality. Like the GGA functional, the meta-GGA is also semi-local in exchange-correlation, and it is defined as follow:

$$E_{xc}^{\text{MTGGA}} [n_{\uparrow}, n_{\downarrow}] = \int d\mathbf{r} \varepsilon_{xc}^{\text{MTGGA}}(n_{\uparrow}, n_{\downarrow}, \nabla n_{\uparrow}, \nabla n_{\downarrow}, \tau_{\uparrow}, \tau_{\downarrow}) \quad (1)$$

The main supplementary ingredient of E_{xc}^{MTGGA} , with respect to the GGA one, is the positive kinetic energy densities $\tau_{\sigma}(\mathbf{r})$, where $\sigma = \{\uparrow, \downarrow\}$ is the spin index³⁴. Being implicit functionals of the electron densities $n_{\sigma}(\mathbf{r})$, they kinetic densities are constructed from the Kohn-Sham orbitals :

$$\tau_{\sigma}(\mathbf{r}) = \sum_i^{\text{occ}} \frac{1}{2} |\nabla \phi_i^{\sigma}(\mathbf{r})|^2 \quad (2)$$

Notice that in addition, the Laplacians of the electron densities $\nabla^2 n_{\sigma}(\mathbf{r})$, can be incorporated into the meta-GGA functionals³⁵.

Several parameterizations of the meta-GGA exist in literature, where the well known are the TPSS of Tao and coworkers³⁶, its revised version rev-TPPS³⁷, M06L³⁸ and mBJ³⁹. The recently proposed one, namely the strongly constrained and appropriately normed (SCAN) functional⁴⁰, has attracted much attention. According to the authors, the most important ingredient making the SCAN superior to previous meta-GGA functionals, is the dimensionless parameter of the kinetic energy densities:

$$\alpha = \frac{\tau_{\sigma}(\mathbf{r}) - \tau_{\sigma}^{\text{W}}(\mathbf{r})}{\tau_{\sigma}^{\text{unif}}(\mathbf{r})} > 0, \quad (3)$$

This parameter is capable to distinguish three different bonding characters: covalent ($\alpha = 0$), metallic ($\alpha = 1$) and weak ($\alpha \gg 1$). A variety of SCAN calculations on diverse molecular and extended systems have been reported⁴¹⁻⁴⁵. They have demonstrated that this functional leads to very interesting results, especially for structural geometry and energetics⁴³⁻⁴⁵. Moreover, it is argued that SCAN functional could be suitable (at least qualitative) for the treatment of strong correlations^{46,47}, and the related ground-state symmetry breaking⁴⁸. We notice finally that two revised formulation of the SCAN functional, known as rSCAN⁴⁹ and r2SCAN⁵⁰, are also available.

B. Hybrid (Hartree-Fock)-DFT

One of the outstanding improvements on the DFT exchange-correlation field is the *hybrid* functionals. The basic idea, proposed initially by Becke^{51,52}, is to mix a fraction of the non-local exact exchange (Hartree-Fock exchange) into the local or semi-local DFT E_{xc} . He then suggested the simple choice of a linear combination:

$$E_{xc}^{\text{Hybrid}} = E_{xc}^{\text{GGA}} + \alpha (E_x^{\text{HF}} - E_x^{\text{GGA}}) \quad (4)$$

where α is a parameter obtained empirically by some fitting of the atomization energies. A later improved version, the B3LYP functional⁵³, has become one of the most popular in quantum chemistry. A subsequent step has been undertaken by introducing the PBE0 functional⁵⁴ (described by the authors as a parameter-free functional). Based on the well known GGA-PBE⁵⁵, it is derived from equation 4 with a predefined fraction of Hartree-Fock (HF) exchange $\alpha = \frac{1}{4}$ (justified with some general analysis from perturbation theory⁵⁶):

$$E_{xc}^{\text{PBE0}} = E_{xc}^{\text{PBE}} + \frac{1}{4} (E_x^{\text{HF}} - E_x^{\text{PBE}}) \quad (5)$$

While the previous functionals belong to the family of *global* hybrid functionals, an important advance in this field has been achieved by the so-called *range-separated* hybrid functionals. Due to the long-range nature of the Coulomb interaction, the computation of the HF exact exchange is highly expensive. Heyd *et al.*^{57,58} proposed the use of a *screened* interaction, obtained via a range separation, instead of the bare Coulomb interaction. This idea is very appealing for extended systems, not only technically but also physically. On one side, as emphasized by the authors, the use of a *screened* interaction renders the HF exchange tractable. On the other side, it has been demonstrated that the bare Coulomb interaction in solids is actually screened (within the random-phase approximation^{59,60}, the Coulomb interaction is found to decay like a Yukawa-type potential).

In HSE hybrid functionals (HSE03⁵⁷ and HSE06⁵⁸), the range-separation (and the screening as a result) is achieved by an error function that decomposes the bare Coulomb potential into a short-range (SR) and a long-range (LR) parts:

$$\frac{1}{r} = \underbrace{\frac{1 - \text{erf}(\omega r)}{r}}_{\text{SR}} + \underbrace{\frac{\text{erf}(\omega r)}{r}}_{\text{LR}} \quad (6)$$

where ω represents an adjustable screening parameter. Initially ω was set to 0.15 in HSE03, and then corrected to two different values in subsequent HSE06. However, a unique optimized value can be adopted (see reference⁶¹). The HSE exchange-correlation functional is expressed as:

$$E_{xc}^{\text{HSE}} = \frac{1}{4} E_x^{\text{HF-SR}} + \frac{3}{4} E_x^{\text{PBE-SR}} + E_x^{\text{PBE-LR}} + E_c^{\text{PBE}} \quad (7)$$

As it can be seen, the GGA-PBE and the PBE0 hybrid functional are merely restored, from the two particular values $\omega = \infty$ and $\omega = 0$, respectively.

The correlation energy part E_c^{PBE} (not affected by the separation) is computed at the GGA-PBE level. The same applies for the long-range part $E_x^{\text{PBE-LR}}$ and for 75% of the short-range part $E_x^{\text{PBE-SR}}$. Thus, one is only left with 25% of the short-range part $E_x^{\text{HF-SR}}$ which needs to be calculated exactly. However, even with these simplifications, the latter remains computationally very expensive. It is defined as:

$$E_x^{\text{HF-SR}} = -\frac{1}{2} \sum_{\sigma} \sum_{n,\mathbf{k}} \sum_{n',\mathbf{k}'} \int \int d\mathbf{r} d\mathbf{r}' (1 - \text{erf}(\omega|\mathbf{r} - \mathbf{r}'|)) \times \frac{\phi_{n,\mathbf{k}}^{\sigma*}(\mathbf{r}) \phi_{n',\mathbf{k}'}^{\sigma}(\mathbf{r}) \phi_{n',\mathbf{k}'}^{\sigma*}(\mathbf{r}') \phi_{n,\mathbf{k}}^{\sigma}(\mathbf{r}')}{|\mathbf{r} - \mathbf{r}'|} \quad (8)$$

An other progress in this domain is the recently invented PBE0r *local* hybrid functional⁶². Here, a new and completely different approach has been followed. The Kohn-Sham orbitals are expanded in a minimal basis of localized atom-centered tight-binding orbitals. This minimal basis is used to calculate three different terms:

- The onsite HF exchange which acts between states centered on the same site, including the interaction between core and valence ones. It affects mainly the degenerate states by splitting them into a filled and empty band (the well known Mott-Hubbard bands separation in the narrow and partially filled *d* and *f* atomic shells).
- The so-called *bond-exchange*, describing the inter-site exchange interaction occurring between the electron densities in two neighboring atoms involved in chemical bonds. This term is very important for covalent material, and it differs for bonding or antibonding states.
- The long-range exchange acting over distances longer than bond lengths. This term could produce an unphysical behavior in metallic solids, due to the long-range tail of the Coulomb interaction (in the limit of free-electron gas, it leads to a zero density of states at the Fermi level). When the screening is taken into account, such behavior can effectively disappear.

The PBE0r functional can be undoubtedly considered as a range-separated one. In one hand, the use of localized tight-binding orbitals defines naturally a cutoff for the exchange interaction. On the other hand, the neglect of the long-range exchange makes it able to capture the important physical effects originating from screening.

In addition, if the bond exchange is omitted, the E_{xc}^{PBE0r} becomes a *purely local* (i.e. onsite) hybrid functional. In this case, the functional is defined as:

$$E_{xc}^{\text{PBE0r}} = E_{xc}^{\text{PBE}} + \sum_{n=1}^N a_n (E_{x,n}^{\text{HF-onsite}} - E_{x,n}^{\text{PBE-onsite}}) \quad (9)$$

The sum runs over the N atomic species of the system (i.e. the cell used in calculations), where a_n represents the mixing factor of the HF exchange. The PBE0r functional offers a very interesting flexibility, not present elsewhere. The mixing factor a_n which determines the exact HF fraction can differ from an atomic species to another in the system. Moreover, the *bond* exchange can be included or not, depending on the physics one aims to describe. For example, in band insulators and covalent compounds (like silicon), this term is necessary to open a band gap; while it is not in the case for Mott-Hubbard insulators.

C. Hubbard corrected DFT

In this section, we review briefly some of the basic notions of the Hubbard-corrected DFT methods. We concentrate on the recently proposed DFT+ U + V formalism⁶³ (using the extended Hubbard model), from which the simplified and extensively used DFT+ U ^{64–66} (either LDA+ U or GGA+ U) can be straightforwardly obtained. Starting from any local or semi-local exchange-correlation functional, the corresponding DFT+ U + V one is written as:

$$E_{xc}^{\text{DFT}+U+V} = E_{xc}^{\text{DFT}} + E_{xc}^{U+V} \quad (10)$$

Following the definitions as well as the notations adopted in references^{63,67}, the Hubbard correction to the exchange-correlation energy (in the simplified rotationally-invariant formulation) is given by:

$$E_{xc}^{U+V} = \frac{1}{2} \sum_I \sum_{\sigma mm'} U^I (\delta_{mm'} - n_{mm'}^{II\sigma}) n_{m'm}^{II\sigma} - \frac{1}{2} \sum_I \sum_{J \neq I} \sum_{\sigma mm'} V^{IJ} n_{mm'}^{IJ\sigma} n_{m'm}^{JI\sigma} \quad (11)$$

where U^I and V^{IJ} are, respectively, the onsite and the intersite Hubbard parameters; and the indices I and J run over all the atomic sites. Notice that the sum over J in the second line, covers the all neighboring atoms desired to be included in the intersite correction.

In equation 11, the onsite occupation matrix elements $n_{mm'}^{II\sigma}$ are obtained by the projection of the Kohn-Sham states $|\psi_{\mathbf{k}\nu}^\sigma\rangle$ on a set of localized (atomic) orbitals $|\phi_m^I\rangle$. Its generalization, involving two localized orbitals centered on two different atomic sites, gives the expression of intersite occupation matrix elements, which reads as:

$$n_{mm'}^{IJ\sigma} = \sum_{\mathbf{k}\nu} f_{\mathbf{k}\nu}^\sigma \langle \psi_{\mathbf{k}\nu}^\sigma | \phi_m^J \rangle \langle \phi_m^I | \psi_{\mathbf{k}\nu}^\sigma \rangle \quad (12)$$

where $f_{\mathbf{k}\nu}^\sigma$ represent the occupations of the Kohn-Sham states, ν is the electronic band index and \mathbf{k} is the Bloch wave vector (in the first Brillouin zone). The localized orbitals (to which the Hubbard correction is applied) are usually the d or f atomic states. The m (m') index is the magnetic quantum number, running over the orbital momentum in atom I (J). Notice that the onsite occupation elements $n_{mm'}^{II\sigma}$, can be obtained as a particular case ($I = J$) in the equation 12.

Before closing this section, one needs to mention the important issue about the values of the U and the V Hubbard parameters. These latter are actually unknown, and they are usually tuned by hand in order to reproduce some desired experimental data (like lattice constants, magnetic moments and more importantly band gaps). Such a procedure, however, makes partially the

DFT+ U + V an empirical method and not completely *ab-initio* one. In this context, there exist several first-principles techniques, aiming to compute the correct values of U and V . Some of the well known are, the constrained DFT (cDFT)^{68–70} and the constrained random-phase approximation (cRPA)^{71–73}. A recent one, using density-functional perturbation theory (DFPT)^{74,75}, has been elaborated with a main advantage of a significant reduction in the computational cost in calculating these Hubbard parameters.

Last but not least, it is also important to notice that these Hubbard parameters intimately depend on the chemical environment from which they are computed. In other terms, they are not transferables and they should never be taken as universal for a given atomic species⁷⁶. In addition, the Hubbard correction depends of the kind of the Hubbard projector functions that can be chosen differently^{77,78}.

III. COMPUTATIONAL DETAILS

The first principles calculations were based on density functional theory^{32,33}. The exchange-correlation effects are accounted for by three different levels of approximations. First, we started by the standard generalized gradient approximation (GGA) in the PBESol parameterization⁷⁹; and the SCAN meta-GGA functional⁴⁰. Then, in a second step two different range-separated hybrid functionals are employed, the HSE06 functional⁵⁸ and the PBE0r one^{62,97,99}. Finally, the mean-field DFT+ U + V approach proposed by Campo *et al*⁶³ has been used. As concern the double counting correction (inherent to the DFT+ U framework), this formulation belongs to the so-called *fully localized limit* family^{65,80–82}. The basic underlying theory is summarized in the previous section II. Two different computational codes, implementing all these methods, are employed in the present work.

The PBESol, SCAN, HSE06 and DFT+ U + V calculations were performed using the plane-wave pseudopotential (PW-PPs) method as implemented in the Quantum ESPRESSO (QE, version 7.1) package.^{83–85} In the PBESol, HSE06 and DFT+ U + V cases, the Kohn-Sham single-particle equations were solved within the projector-augmented wave (PAW) method⁸⁶. The used PAW potentials are taken from the PSLibrary⁸⁷ (Mn.pbesol-spn-kjpaw.ps1.0.3.1.UPF and C.pbesol-n-kjpaw.ps1.1.0.0.UPF). In the SCAN meta-GGA, however, the norm-conserving PP's from the PseudoDojo library⁸⁸, have been used (meta-GGAs are not yet implemented for PAW potentials and ultra-soft PP's in QE package).

To compute of the onsite U and intersite V Hubbard parameters, we have used the HP code⁸⁹; which is a part of the QE package. The corresponding linear-response calculations are carried out using a self-consistent DFPT approach, with an increased uniform Γ -centered \mathbf{q} -point mesh until $3 \times 3 \times 3$. The orthogonalized atomic

orbitals have been used as Hubbard projectors functions, constructed by means of Löwdin orthogonalization method^{77,89,90}. More information on the HP code and its technical details can be found in Reference⁸⁹. We emphasize that since these parameters are not transferables, they are computed separately for the rocksalt and the zincblende crystal structures. Moreover, in each crystal structure, they are recalculated again at every volume step in the energy versus volume optimization of MnC cell.

All calculations were converged with a plane-wave kinetic-energy cutoff of 50 Ry, until the total-energy difference between two consecutive iterations was lower than 10^{-8} Ry. In the self-consistency calculations, the Brillouin zone was sampled, using a Monkhorst-Pack⁹¹ \mathbf{k} -point mesh of $18 \times 18 \times 18$. For the electronic densities of states calculations, however, Brillouin zone integrations were performed using the improved linear tetrahedron method⁹². To treat metallic ground states, we used the Marzari-Vanderbilt smearing⁹³ with a broadening parameter of 0.02 Ry.

The PBE0r hybrid functional calculations were carried-out using the PAW method⁸⁶, within its original implementation as provided in the Car-Parrinello projector augmented-wave (CP-PAW) code⁹⁴. We recall that PAW is by construction an *all-electron* electronic structure method, using augmented-waves (like the well known LAPW method, but with a different augmentation procedure). The included orbitals in the PAW augmentation are the $2s$, $2p$, and $3d$ of C; and the $3s$, $3p$, $3d$, $4s$, and $4p$ of Mn. In addition, the $3s$, $3p$ semi-core states of Mn were treated as valence orbitals. The covalent radii of the atomic species were set to 0.71 Å for C and 1.17 Å for Mn. The auxiliary partial waves were constructed using matching radii of 0.7 (in units of the covalent radii) for all orbitals. As mentioned previously in section II B, PBE0r uses a localized tight-binding orbitals basis. The latter includes the $2s$ and $2p$ orbitals of C, and the $3s$, $3p$, $3d$, and $4s$ ones of Mn.

In the CP-PAW code, the calculation scheme is the Car-Parrinello *ab initio* molecular dynamics method (AIMD)⁹⁵. The electronic ground-state is reached by applying a friction term (a damped MD) which quenches the system to the ground-state. Here also, and to be in line with previous QE calculations, a plane-wave kinetic-energy cutoff of 50 Ry for the auxiliary wave functions was used. The Brillouin zone integration was performed using the improved linear tetrahedron method⁹², with up to $7 \times 7 \times 7$ \mathbf{k} -point mesh, leading 200 \mathbf{k} -points. The total energy was minimized up to a convergence threshold of 10^{-5} Hartree. To deal with the variable occupations of the one-electron energy eigenstates, mandatory for metallic systems, the Mermin functional⁹⁶ has been used.

While SCAN and PBESol have nearly the same computational cost, the hybrid PBE0r is a bit more demanding but still comparable to them^{30,97-100}. However, as mentioned earlier in section II B, the HSE06 calcula-

tions are too expensive; especially with plane-waves⁶⁷. In HSE06 calculations, we have used two fractions of short-range HF exchange, 10% and 20%; with a uniform \mathbf{q} -point mesh of $3 \times 3 \times 3$. Concerning the HF mixing factor of the PBE0r, and for sake of consistency, we also used two values 0.1 and 0.2 (corresponding respectively to 10% and 20% fractions). The same value has been assigned for both C and Mn atomic species.

IV. GROUND-STATE CRYSTAL STRUCTURE AND MAGNETIC ORDER

Structural stability of MnC is investigated in the two faces-centered cubic rocksalt (RS) and zincblende (ZB) structures. This choice is motivated by the fact that all known monoxides, mononitrides and monocarbides are found to crystallize in these two structures. Theoretical ground-state is obtained from the energy versus volume optimization. The corresponding calculations are carried out within both spin-polarized ferromagnetic (FM) and antiferromagnetic (AF) solutions. We considered the type-II antiferromagnetic (AFII) (well known in the transition metal monoxides MnO, NiO etc.), which consists on alternating ferromagnetic plans along the $\langle 111 \rangle$ direction.

As an aside note, we mention that additional calculations, for MnC in wurtzite structure, have been performed for sake of completeness. The latter crystal structure was found to be the most unstable one. Thus, the corresponding results are omitted in the present paper.

TABLE I. The calculated total energies differences (in Ryd) between rocksalt (RS) and zincblende (ZB) structures, at theoretical equilibrium; as arising from all the frameworks.

	$E_{RS} - E_{ZB}$
PBESol	- 0.028
SCAN	+ 0.035
PBE0r	+ 0.043
HSE06	- 0.045
DFT+U+V	- 0.028

The obtained results from PBESol, SCAN, HSE06 and DFT+U+V are shown in Fig. 1, where the curves have been fitted with the third-order of Birch-Murnaghan equation of state¹⁰¹. Similarly, Fig. 2 gives those arising from PBE0r functional. The main important result about the structural stability of MnC, is that SCAN and PBE0r functionals outdo the three others schemes; being the only methods reproducing the experimental finding i.e. a ground-state zincblende structure. The calculated differences in total energies at equilibrium (between the rocksalt and the zincblende structures) are provided in Tab I. In fact, the zincblende structure has a lower total energy within SCAN and PBE0r functionals. It is important to mention here that for the PBE0r functional, only

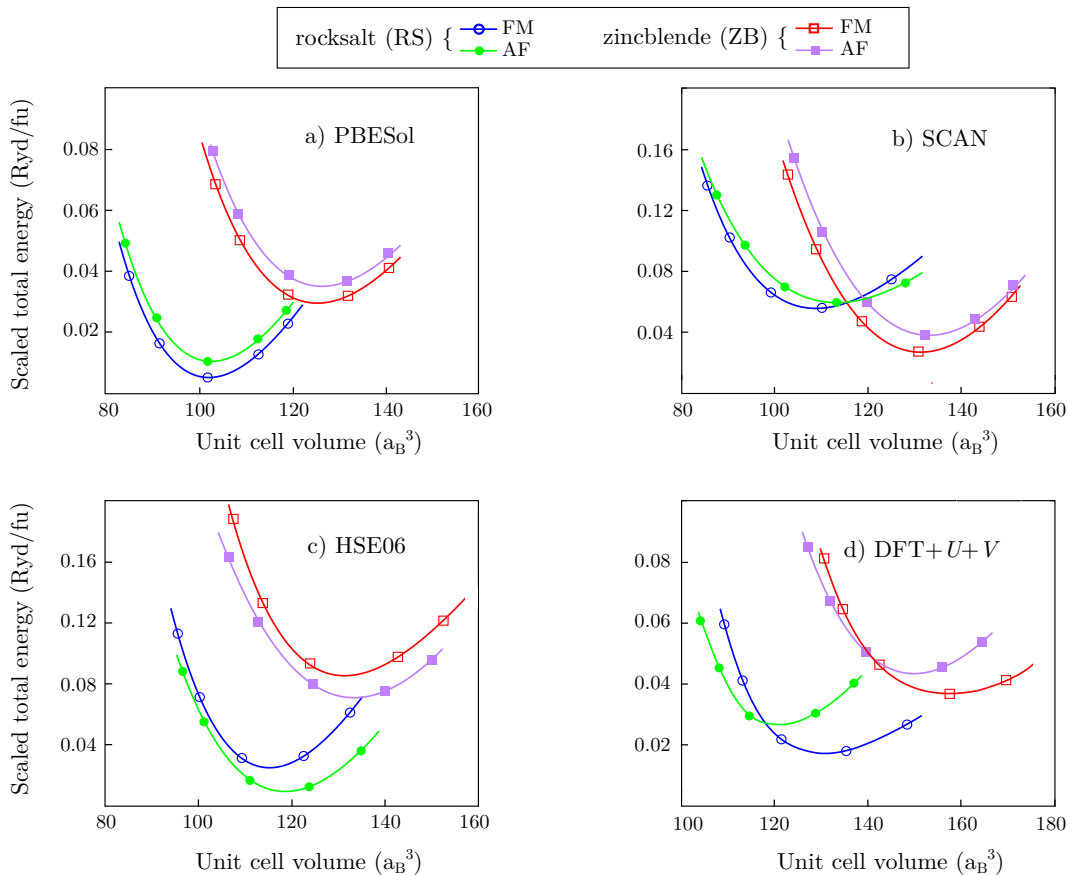


FIG. 1. Energy versus volume optimization of MnC in rocksalt (RS) and zincblende (ZB) structures; as obtained within: a) PBESol, b) SCAN, c) HSE06 and d) DFT+ $U+V$ functionals.

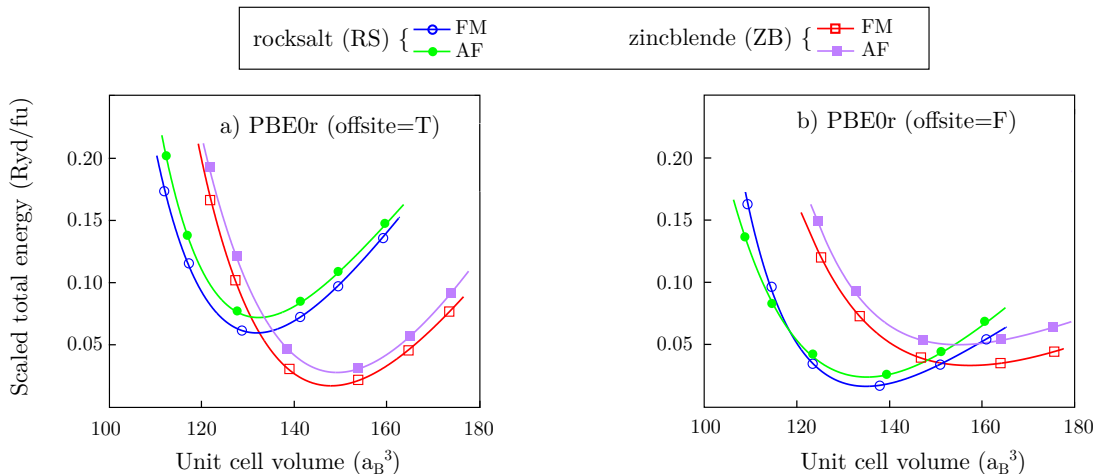


FIG. 2. Energy versus volume optimization of MnC in rocksalt (RS) and zincblende (ZB) structures; as obtained within PBE0r functional: a) PBE0r (offsite=T) with the bond exchange, and b) PBE0r (offsite=F) without the bond exchange.

a 10% fraction of the HF exact exchange was sufficient to reproduce correctly the experimental stability.

As it is clear from Fig. 1, GGA and HSE06 as well as DFT+ $U+V$ all fail to predict the correct ground-state structure. Such a failure of the GGA framework is actu-

ally not new, and it has been reported in several other cases, such as in neighboring MnN compound^{10,14,105}. In the latter case, however, hybrid functionals as well as GGA+ U approaches were able to lift this discrepancy¹². Surprisingly here, neither the usually accurate HSE06

TABLE II. Calculated equilibrium properties within PBEsol, SCAN, PBE0r and HSE06 hybrid functionals, as well as the mean field DFT+ $U+V$; for MnC in rocksalt (RS) and zincblende (ZB) structures. The lattice constant a in Å, the magnetic moment per formula unit M_{fu} in μ_{B} (in the FM case) and the bulk modulus B in GPa are shown.

	RS			ZB		
	a	B	M_{fu}	a	B	M_{fu}
<u>PBEsol</u>						
FM	3.97	230	1.15	4.22	172	1.00
AF	3.98	232		4.23	166	
<u>SCAN</u>						
FM	4.02	224	1.30	4.28	175	1.00
AF	4.08	219		4.31	169	
<u>PBE0r</u>						
FM	4.15	214	2.88	4.44	192	2.05
AF	4.17	210		4.48	150	
<u>HSE06</u>						
FM	4.10	238	2.58	4.32	201	1.94
AF	4.14	220		4.35	189	
<u>DFT+$U+V$</u>						
FM	4.27	211	3.04	4.51	116	3.00
AF	4.17	204		4.44	102	
<u>Theory</u>						
Ref. ²⁴	4.02	295		4.31	240	
Ref. ²⁷				4.23		
Ref. ²⁹				4.20		
<u>Experimental</u>						
Ref. ²⁶				4.43	170	

functional (with up to 20% of the HF exact exchange) nor the DFT+ $U+V$ method are able to stabilize the MnC zincblende structure.

Before inspecting some of the physical properties at equilibrium, let's first analyze and explain further this stability issue. Concerning SCAN functional, its main advantage is the ability to recognize the different types of bonding. It has been confirmed from an extensive benchmark calculations⁴³ (up to 1000 crystalline compounds known experimentally), that the errors in the formation energy for strongly bound compounds are substantially decreased ($\sim 50\%$ compared to GGA-PBE). The reason behind this success is due to the enhanced exchange interaction in the covalent bonding regime^{39,43}.

To address and understand more this result, we took advantage from the flexibility of PBE0r framework, by performing two kind of calculations. First, the results of calculations including the *bond* exchange are shown in Fig. 2 (a) (denoted by *offsite*=T, and which refers to the *offsite* terms of the exact exchange interaction describing the exchange along the bond). Oppositely, calculations without the *bond* exchange i.e. with only *onsite* exchange terms, have been carried out and the results are shown in Fig. 2 (b) (denoted by *offsite*=F). Clearly, tacking into account the *bond* exchange turns out to be crucial in stabilizing the zincblende structure; and ignor-

ing it renders the rocksalt one more stable. As mentioned above in section II B, the *bond* exchange has the characteristic to distinguish between bonding and antibonding states, and acts differently for their occupations. Thus, it describes better the covalency effects of the chemical bond, reducing again the formation energy errors. In view of the agreement between the two schemes, one can argue that the SCAN exchange interaction enhancement plays a similar role to the PBE0r *bond* exchange; with the latter constituting a more systematic description of the interaction in the chemical bond.

We believe that the failure of the HSE06 functional can be explained as follow. On one hand, it is built upon GGA-PBE which is by construction enable to recognize the weak, covalent and metallic bonding regimes. On the other hand, the exact exchange is added as a whole fraction. That is to say, HSE06 does not have a particular part of the exchange (like the *bond* exchange of PBE0r), that differentiates bonding and anti-bonding states. As a result, this sole addition of the exact exchange to GGA-PBE turns out to be insufficient to cure the formation energy errors. The same arguments hold as well for the deficiency of the DFT+ $U+V$ method.

In Tab. II, we summarize the calculated values of the lattice parameters (in Å), the bulk moduli (in GPa) and the magnetic moments per formula unit M_{fu} (in μ_{B}). For

the latter, we only show the moments in the case of the ferromagnetic order, since it is more stable than the antiferromagnetic one (see discussion below).

First of all, we remind that the only available experimental data are those reported recently on zincblende MnC²⁶. In this case, PBESol and SCAN are found to underestimate the lattice constant value, and oppositely DFT+ U + V overestimates it. On the other side, hybrid functionals are giving more closer values to experiments, in particular PBE0r for which the agreement is nearly perfect. As far as we know, MnC has never been elaborated in the rocksalt structure, and our PBESol results agree very well with the few previous GGA calculations^{23,24}. A different situation is found for the calculated values of the bulk moduli. Here, the agreement with experiments²⁶ is obtained within semi-local functionals; while hybrid functionals tend to an overestimation and DFT+ U + V method seems to underestimate it.

Turning to the magnetic stability, all frameworks agree that the ferromagnetic ordering is favored over the type-II antiferromagnetic one; in the two crystal structures. The only exception arises within HSE06 where the latter is more stable. According to the computed values of the magnetic moment per unit cell, as shown in Tab II, one important point could be noticed. The PBESol, SCAN and DFT+ U + V methods have led to an integer values in the zincblende structure. Such feature could constitute a signature of a half-metallic ferromagnetism, as already pointed out in literature. This point will be confirmed below when discussing in more detail the MnC electronic structure, through the electronic densities of states.

V. ELECTRONIC STRUCTURE AND BONDING PROPERTIES

In this section, we give a detailed description of the electronic structure and chemical bonding properties. This is done through the site-, orbital-, and spin-resolved densities of states (PDOS), as computed in the different functionals. In addition, we concentrate on the ground state spin-polarized ferromagnetic case; which could also be more relevant for practical applications.

A. Semi-local PBESol and SCAN

In a first step, the MnC electronic structure is explored within GGA-PBESol, where the obtained densities of states are shown in Fig. 3. Here and in the following discussions, to explicitly account for the effects of the crystal field (octahedral in rocksalt and tetrahedral in zincblende), the Mn $3d$ -states are splitted into Mn- t_{2g} and Mn- e_g manifolds. In general, there are three main regions corresponding to bonding, non-bonding and anti-bonding states. Notice that the s states, which lie in a low energy window, are omitted in the figures.

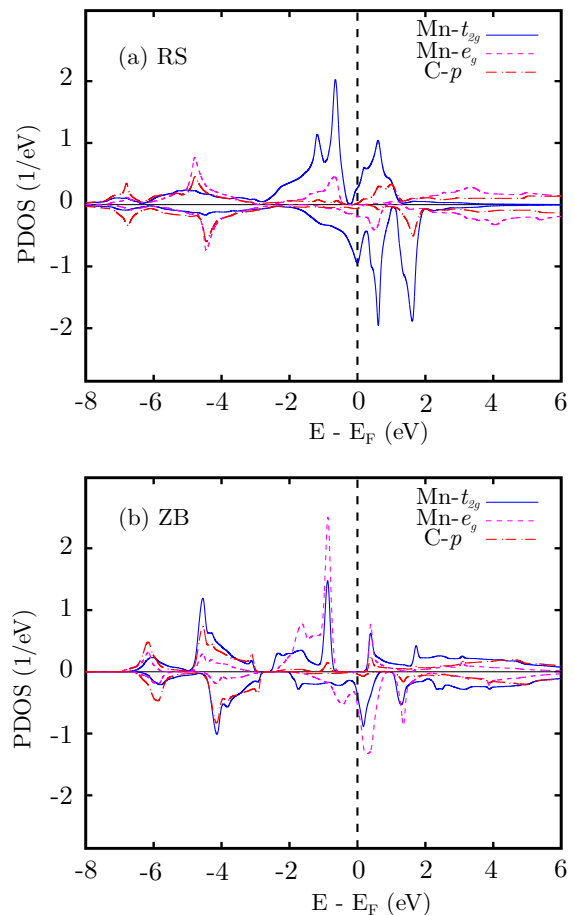


FIG. 3. Atom- and spin-resolved densities of states (PDOS) of MnC in RS-type (a) and ZB-type (b) structures, as arising from the PBESol spin-polarized FM calculations.

For the rocksalt structure, shown in the upper panel of Fig. 3; the bonding region is located in the energy interval $[-8 \text{ eV}, -3 \text{ eV}]$ formed by the Mn- e_g and the C- p states (a strong σ -type overlap caused by the octahedral arrangement). A small contribution from the Mn- t_{2g} is also visible. Next, one can find the non-bonding part dominated by the Mn- t_{2g} manifold from -3 eV to $+1 \text{ eV}$. In the higher energy window, the hybridization of Mn- e_g and C- p states forms the anti-bonding counter-part. Here, MnC has clearly a metallic behavior. The exchange splitting indicates that the magnetic moment arises principally from the Mn- t_{2g} states, with a small contribution from the Mn- e_g ones. A large part of these states are located above the Fermi level, indicating a low-spin configuration. This is consistent with the computed value ($\sim 1.45 \mu_B$) of the magnetic moment.

In the zincblende structure, the Mn- d states separation is obviously inverted due the tetrahedral environment; but the situation here is considerably different form the previous one. As displayed in the lower panel of Fig. 3, the strong σ -type hybridization between the Mn- t_{2g} and the C- p states gives rise to the bonding region in the energy interval of $[-6 \text{ eV}, -3 \text{ eV}]$. While the C- p states

dominate the bottom of this region (around -6 eV), they contribute almost equally with Mn- t_{2g} states in the rest of this bonding zone. Moving higher in energy, the non-bonding region is dominated by the two Mn- e_g bands, but with a substantial contribution of Mn- t_{2g} . Finally, the anti-bonding region above +1.5 eV, contains essentially C- p and Mn- t_{2g} hybrid states. This large separation between bonding and anti-bonding parts of the Mn- t_{2g} manifold indicates the high strength of the Mn-C bond.

More importantly, zincblende MnC is insulating in the majority-spin channel (see the position of the Fermi level in Fig. 3 (b)), while being metallic in the minority-spin one. This makes MnC a ferromagnetic half-metal with a majority-spin band gap of about ~ 1.2 eV. This electronic structure result is in perfect agreement with those reported elsewhere²⁷⁻²⁹.

Next, we turn to the electronic densities of states as computed from the SCAN meta-GGA. The results shown in Fig. 4 indicate a very similar picture to the PBEsol one, even-though the two functionals have led to different ground state structure (see section IV above). Actually, this is not a discrepancy in the performance of SCAN functional, and there is no a contradiction between the two kind of results. Most of the studies available in literature, have already pointed out that SCAN, and all other meta-GGA functionals, do not really improve over GGA for electronic and magnetic properties; such as band gaps, magnetic moments (for a overall assessment on the performance of SCAN functional, see for example references^{43,45,47}).

Here also, MnC is predicted as a ferromagnetic, metal in rocksalt structure and a half-metal in zincblende one (with a majority spin band gap). The whole distribution of the DOS is very similar to the PBEsol one, where the different bonding, non-bonding and anti-bonding regions are nearly located in the same energy windows. The only important difference, with respect to PBEsol, concerns the zincblende structure. The Fermi level is pushed upward at the vicinity of a non-vanishing DOS, making the compound at the verge of being completely metallic. This point has been already mentioned previously^{27,28}, where a small increase in the lattice constant has driven the compound to become fully metallic. Consequently, this confirms the finding that under expansion, the zincblende MnC becomes a pure metal²⁸.

B. Hybrid PBE0r and HSE06

After a semi-local DFT description, we turn now to the effect of the non-local exact exchange on the MnC electronic structure; as partially included within hybrid functionals. As mentioned above in section III, we used two fractions (10% and 20%) of the HF exact exchange. Both of the values have led to similar electronic properties results, such as the metallic character for MnC (in rocksalt as well as zincblende structures). In addition, the whole distribution of the electronic PDOS (the bond-

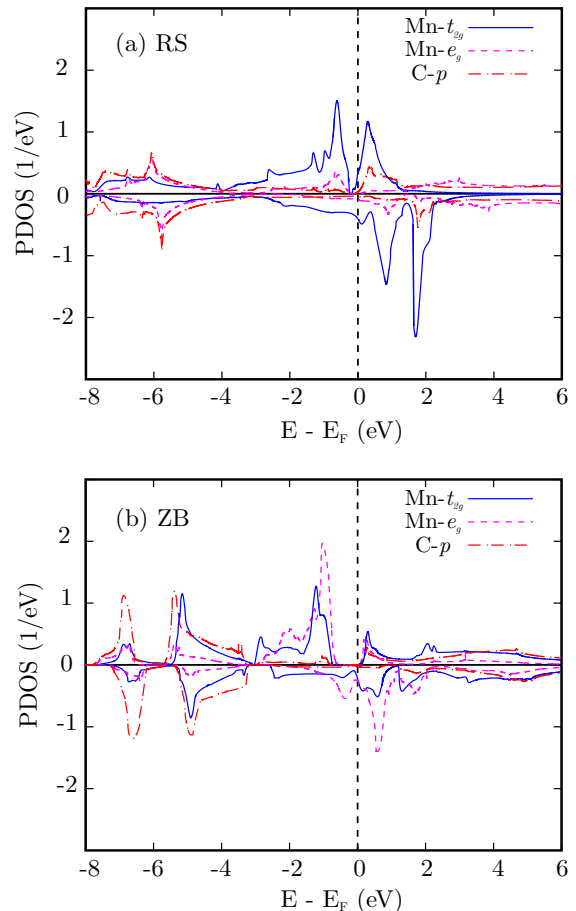


FIG. 4. Atom- and spin resolved densities of states (PDOS) of MnC in RS-type (a) and ZB-type (b) structures, as arising from the SCAN spin-polarized FM calculations.

ing, non-bonding and anti-bonding regions) and the Mn-C hybridization resemble fairly with the two fractions. The only notable difference is that a larger fraction (20%) produces larger magnetic moments, due to the enhanced exchange splitting.

The electronic site-, orbital-, and spin-resolved densities of states obtained from PBE0r and HSE06 frameworks are displayed in Fig. 5 and Fig. 6, respectively; where the two methods agree very well in their predictions. At first sight, the main effect produced by the exact exchange is the larger exchange splitting; in particular for the Mn- d states.

In the rocksalt structure, the shape as well as the distribution of the DOS (bonding, non-bonding and anti-bonding regions) closely resemble those of PBEsol and SCAN semi-local functionals. A clear difference, however, is the downshift (upshift) of the non-bonding Mn- t_{2g} states in the majority (minority) spin channel. In PBE0r framework the corresponding shifts are very important, so that the majority spin states are almost filled; and the minority spin ones are almost empty. This drives the Mn- t_{2g} manifold (three-fold degenerate) to a quasi high-spin configuration, whereby the value of the mag-

netic moment ($\simeq 3 \mu_B$, see Tab. II). In HSE06, a similar situation is found but with a slightly less important shifts.

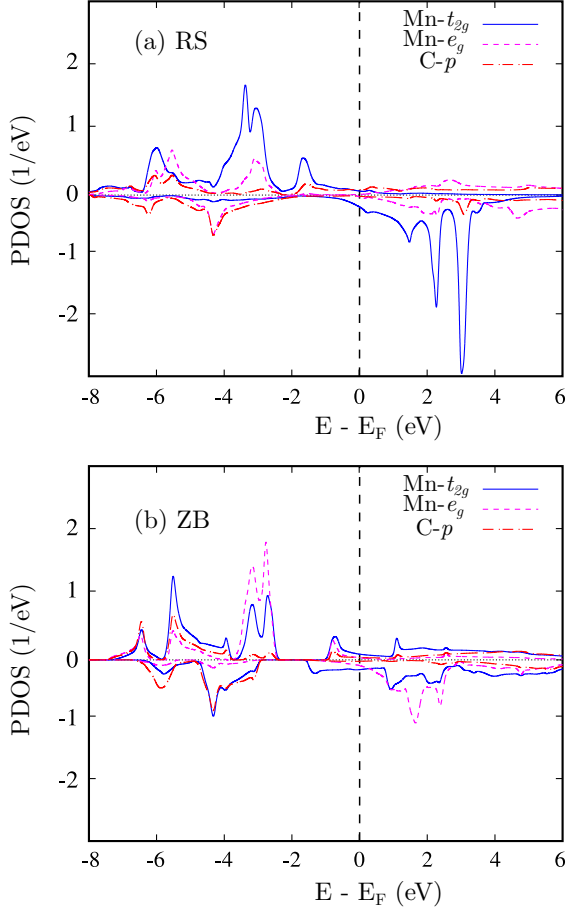


FIG. 5. Atom- and spin resolved densities of states (PDOS) of MnC in RS-type (a) and ZB-type (b) structures, as arising from the PBE0r, with *bond* exchange (offsite=T), spin-polarized FM calculations.

In the zincblende structure, the same description holds for the two hybrid functionals densities of states; with an inverted role between the Mn- t_{2g} and Mn- e_g shells. The latter (two-fold degenerate) being more subjected to the exchange splitting, is also derived toward a high-spin configuration. This is again consistent with the computed values of the magnetic moments.

The important difference between hybrid functionals and semi-local ones, concerns the electronic character of zincblende MnC. As shown in the lower panels of Figs. 5 and 6, the half-metallicity disappears and the compound becomes fully metallic. This result is somewhat expected due to the larger lattice constant of the hybrid functionals (see Tab. II). As mentioned at the end of the previous section, all previous GGA calculations have shown that this behavior is very sensitive to the value of the lattice constant.

In this context, additional PBE0r and HSE06 calculations have been carried out; at the smaller lattice constant obtained from PBESol and SCAN. As a matter of

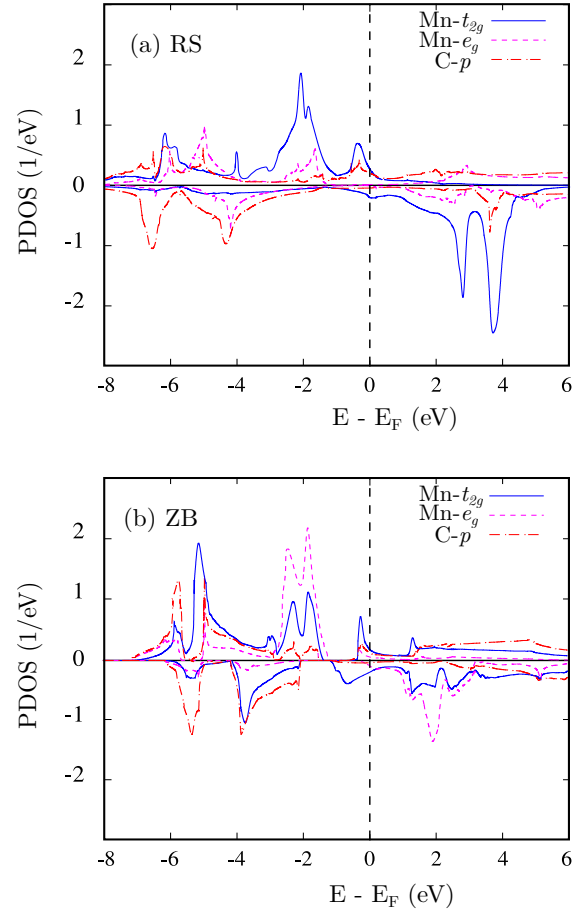


FIG. 6. Atom- and spin resolved densities of states (PDOS) of MnC in RS-type (a) and ZB-type (b) structures, as arising from the HSE06 spin-polarized FM calculations.

fact, the obtained DOS plots (not shown here) show that the compound is truly a half-metal. Consequently, both semi-local and hybrid functionals agree that zincblende MnC exhibit half-metallicity at smaller lattice constants (from 4.2 Å to 4.3 Å); which vanishes under expansion. Yet, and in view of the present results, the compound is expected to be a ferromagnetic metal at the experimental lattice constant (~ 4.4 Å). In the next section, however, we will see that DFT+ U + V method changes radically this picture.

C. Mean field DFT+ U + V

This section is devoted to the electronic structure as arising from the mean field DFT+ U + V , as the last method used in the present investigation. As mentioned earlier in section III, the computation of the onsite U and the intersite V Hubbard parameters has been carried out self-consistently using the linear response DFPT method. The obtained values at theoretical equilibrium are shown in Tab III. For sake of completeness, we also provide the computed values at the PBESol equilibrium, and at the

zincblende experimental lattice constant (4.43 Å). One important point could be noticed, is about strength of the intersite V Hubbard parameter. Indeed, its value is found to decrease when the lattice constant increases (from PBESol, to experimental and then to DFT+ $U+V$). This is obviously expected, since this parameter is meant to describe electronic interaction between the two sites of the Mn-C bond.

TABLE III. The calculated values of the onsite U and the intersite V Hubbard parameters for Mn $3d$ states, in eV, at: DFT+ $U+V$ and PBESol lattice constants; as well as experimental one. The values are for ferromagnetic solution only; in the rocksalt (RS) and zincblende (ZB) structures.

		RS	ZB
a _{DFT+$U+V$}	U	5.60	5.50
	V	0.57	0.70
a _{PBESol}	U	5.93	5.55
	V	0.64	0.81
a _{Exp.}	U		5.43
	V		0.76

As an side remark, the transition metal monoxides (MnO, NiO etc...), widely used as prototypes for strongly correlated systems, generally have an onsite U Hubbard parameter larger than 6 eV^{102–104}. Thus, the smaller ones calculated here let to believe that the static electronic correlations in MnC are less stronger than in the monoxides.

The site-, orbital-, and spin resolved densities of states obtained from the DFT+ $U+V$ method are displayed in Fig. 7. For the rocksalt structure, the results are wholly similar to those obtained with hybrid functionals. The noticeable difference is the exchange splitting of the Mn- t_{2g} shell which is found to be the most important, than in all other schemes. As shown in the figure, those orbitals (three-fold degenerate) are in a complete high-spin configuration, giving rise to the largest computed magnetic moment ($M_{\text{fu}} > 3 \mu_B$).

In the zincblende structure, there is a drastic change compared to all the previous approaches. Unlike with hybrid functionals, the half-metallic character is restored again here. Moreover, the calculated values of the minority-spin band gap (~ 2.5 eV) as well as the magnetic moment ($3 \mu_B$) are substantially enhanced. In contrast to the rocksalt case, it is the two-fold degenerate Mn- e_g orbitals which adopt a high-spin configuration; contributing with $2 \mu_B$ to the total magnetization. The remaining $1 \mu_B$ comes mainly from Mn- t_{2g} states, as can be seen in the lower panel of Fig. 7.

In this case, the semi-local functionals and the mean field DFT+ $U+V$ method are in line in predicting the half-metallicity. There are, however, two important differences about this character between the two frameworks. While the band gap lies within the majority-spin channel in the former, it has now moved to the

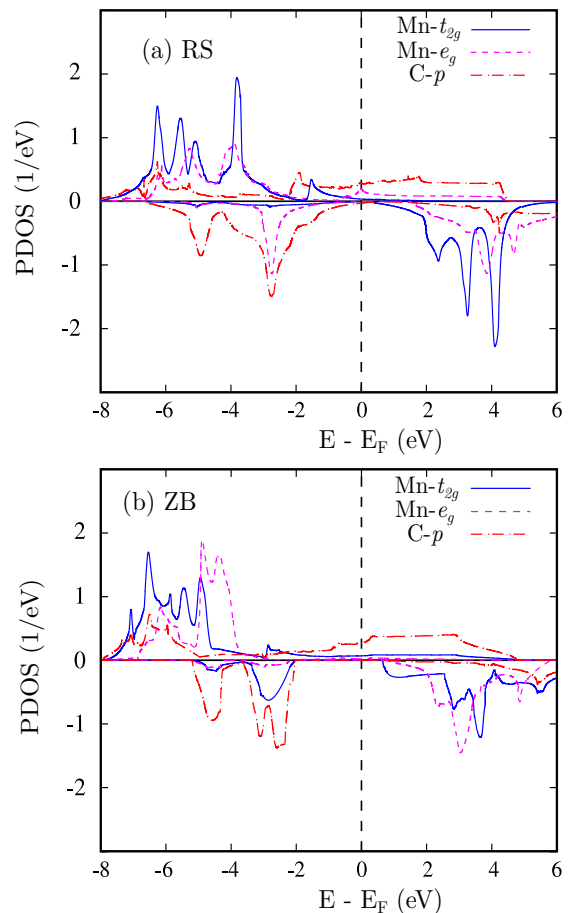


FIG. 7. Atom- and spin resolved densities of states (PDOS) of MnC in RS-type (a) and ZB-type (b) structures, as arising from the DFT+ $U+V$ spin-polarized FM calculations.

minority-spin one. Curiously and more importantly, this behavior occurs in a lattice constant value (4.55 Å) much larger than the limit (≥ 4.30 Å) for which it is supposed to disappear in semi-local functionals. To explore more this contrasting feature, further DFT+ $U+V$ calculations have been carried out; at the experimental lattice constant (4.43 Å) and at the PBESol one (4.22 Å) (using the corresponding calculated Hubbard parameters as listed in Tab. III). As a matter of fact, zincblende MnC remains half-metallic at the experimental lattice constant; whereas it becomes purely metallic at the PBESol equilibrium. Thus, oppositely to the prediction made by semi-local and hybrid functionals, the half-metallicity is vanishing under compression according to DFT+ $U+V$.

It's worthwhile to mention that similar observations have been made for several compounds crystallizing in the fourfold coordinated zincblende structure. Based on GGA calculations, Pask and coworkers²⁸ have shown that many pnictides, such as Mn(Cr)As(Sb) half-metals with minority-spin gap, see their half-metallicity disappear upon compression. In the same work, it was also noticed that the opposite occurs in MnC, being the only half-metal with majority-spin gap.

Unfortunately, no experimental magnetic data on the MnC magnetic properties have been found; to which our results can be confronted. So, at this stage, the issue about the origin, nature and existence of this half-metallic character remains open.

VI. CONCLUSION

The structural, magnetic and electronic properties of manganese monocarbide MnC, in the rocksalt (RS) and the zincblende (ZB) structures, have been investigated. Using the state-of-the-art of DFT based methods: GGA (PBESol), meta-GGA (SCAN), hybrid functionals (PBE0r and HSE06) and mean field DFT+ $U+V$; the following results have been obtained.

The first important result concerns the ground state crystal structure, where only SCAN and PBE0r functionals are capable to reproduce the experimental zincblende structure; in contrast to the others. We believe that the success of the SCAN functional is due to the enhanced exchange in the covalent bonding regime. Moreover, the PBE0r calculations allowed to show explicitly the crucial role played by the so-called *bond* exchange in stabilizing the zincblende structure over the rocksalt one. The semi-local functionals (PBESol and SCAN) are found to underestimate the lattice constant, while the DFT+ $U+V$ tends to an overestimation. It is the hybrid functionals,

however, that give a better agreement with experiment; especially PBE0r. For the magnetic ordering, except the HSE06 functional, all the methods agree on the stability of the ferromagnetic order over the type-II antiferromagnetic one.

The electronic structure and chemical bonding have been analyzed through the densities of states. In the six-fold coordinated rocksalt structure, all the computational schemes predict similar bonding and electronic properties; leading to a pure metallic behavior. A large exchange splitting is found within hybrid functionals, and becomes more important when DFT+ $U+V$ is applied.

For MnC in the fourfold coordinated zincblende structure, a very interesting and contrasting results have been obtained. On one hand, the two hybrid functionals lead to a ferromagnetic metal, at theoretical equilibrium. While both the semi-local functionals (PBESol and SCAN) and the DFT+ $U+V$ method predict MnC as a ferromagnetic half-metal, a major difference exists on the type of this property and its occurrence under pressure. In the former cases, the insulating character is carried by the majority-spin population; in contrast to the latter. Surprisingly, in the semi-local framework (and also hybrid functionals) this half-metallicity vanishes under expansion; while the opposite is happening within DFT+ $U+V$. Yet, in the absence of experimental magnetic data, these contrasting results keep the debate open on the origin and the nature of this behavior.

* corresponding author: abdeslam.houari@univ-bejaia.dz

- ¹ J. H. de Boer and E. J. W. Verwey, Proc. Phys. Soc. **49**, 59 (1937).
- ² N. F. Mott and R. Peierls, Proc. Phys. Soc. **49**, 72 (1937).
- ³ A. Fujimori and F. Minami, Phys. Rev. B **30**, 957 (1984).
- ⁴ A. Fujimori, K. Terakura, M. Taniguchi, S. Ogawa, S. Suga, M. Matoba, and S. Anzai, Phys. Rev. B **37**, 3109 (1988).
- ⁵ G. A. Sawatzky and J. W. Allen, Phys. Rev. Lett. **53**, 2339 (1984).
- ⁶ J. Zaanen, G. A. Sawatzky, and J. W. Allen, Phys. Rev. Lett. **55**, 418 (1985).
- ⁷ A. Leineweber, R. Niewa, H. Jacobs, and W. Kockelmann, J. Mater. Chem. **10**, 2827 (2000).
- ⁸ K. Suzuki, H. Morita, T. Kaneko, H. Yoshida, and H. Fujimori, J. Alloys. Compd. **201**, 11 (1993).
- ⁹ K. Suzuki, T. Kaneko, H. Yoshida, Y. Obi, H. Fujimori, and H. Morita, J. Alloys. Compd. **224**, 232 (1995).
- ¹⁰ K. Suzuki, T. Kaneko, H. Yoshida, Y. Obi, H. Fujimori, and H. Morita, J. Alloys Compounds **306**, 66 (2000).
- ¹¹ A. Houari, S. F. Matar, M. Belkhir Comput. mat. science. **43**, 392 (2008)
- ¹² J. A. Chan, J. Z. Liu, H. Raebiger, S. Lany, and A. Zunger, Phys. Rev. B **78**, 184109 (2008).
- ¹³ A. Houari, S. F. Matar, M. Belkhir and M. Nakhl, Phys. Rev. B **75**, 064420 (2007).
- ¹⁴ M. S. Miao and W. R. L. Lambrecht, Phys. Rev. B **76**, 195209 (2007).
- ¹⁵ H. R. Soni, V. Mankad, S. K. Gupta and P. K. Jha, J. Alloys. Compd. **522**, 106 (2012).
- ¹⁶ H. Wang, and D. S. Xue, Chin. Phys. Lett. **21**, 1612 (2004).
- ¹⁷ C. Paduani, Solid. State. Commun. **148**, 297 (2008).
- ¹⁸ A. Houari, S. F. Matar, and V. Eyert, Electron. Struct. **1** 015002 (2019).
- ¹⁹ D. J. Singh, and B. M. Klein, Phys. Rev. B **46**, 14969 (1992).
- ²⁰ Q. Wang, K. E. German, A. R. Oganov, H. Dong, O. D. Feyta, Y. V. Zubavichush and V. Y. Murzinh RSC. Adv. **6**, 16197 (2016).
- ²¹ J. Häglund, A. Fernandez Guillermet, G. Grimvall and M. Korling, Phys. Rev. B **48**, 11685 (1993).
- ²² G. L. Gutsev, L. Andrews, C. W. Bauschlicher, Theor. Chem. Acc. **109**, 298 (2003).
- ²³ N. J. Szymanski, I. Khatri, J. G. Amar, D. Gall and S. V. Khare J. Mater. Chem. C, **7** 12619 (2019).
- ²⁴ I. Khatri, N. J. Szymanski, B. B̄Dumre, J. ḠAmar, D. Gall, S. V̄Khare Journal. Alloys. and Compounds. **891**, 161866 (2022).
- ²⁵ D. Djurovic, B. Hallstedt, J. von Appen, and R. Dronskowski, CALPHAD. Comput. Coupling Phase Diagrams Thermochem. **34**, 279 (2010).
- ²⁶ A. N. A. Aparajita, N. R. S. Kumar, S. Chandra, S. Amirthapandian, N. V. C. Shekar uand K. Sridhar, Inorg. Chem. **57**, 14178, (2018).
- ²⁷ E. Sasioglu, I. Galanakis, L. M. Sandratskii, and P. Bruno J. Phys. : Condens. Matter. **17**, 3915 (2005).
- ²⁸ J. E. Pask, L. H. Yang, C. Y. Fong, W. E. Pickett, and

- S. Dag Phys. Rev. B **67**, 224420 (2003).
- ²⁹ M. C. Qian, C. Y. Fong, and L. H. Yang Phys. Rev. B **70**, 052404 (2004).
- ³⁰ A. Houari and P. E. Blöchl, J. Phys. : Condens. Matter **30**, 305501 (2018).
- ³¹ W. E. Pickett and J. S. Moodera, Phys. Today **54**, 39 (2001).
- ³² P. Hohenberg and W. Kohn, Phys. Rev. **136**, B864 (1964).
- ³³ W. Kohn and L. J. Sham, Phys. Rev. **140**, A1133 (1965).
- ³⁴ J. P. Perdew, K. Burke, and M. Ernzerhof, AIP Conf. Proc. **577**, 1 (2001).
- ³⁵ J. P. Perdew, S. Kurth, A. Zupan and P. Blaha, Phys. Rev. Lett. , **82**, 2544 (1999).
- ³⁶ J. Tao, J. P. Perdew, V. N. Staroverov, and G. E. Scuseria, Phys. Rev. Lett. **91**, 146401 (2003).
- ³⁷ J. P. Perdew, A. Ruzsinszky, G. I. Csonka, L. A. Constantin, and J. Sun, Phys. Rev. Lett. **103**, 026403 (2009).
- ³⁸ Y. Zhao and D. G. Truhlar, J. Chem. Phys. **125**, 194101 (2006).
- ³⁹ F. Tran, P. Blaha, Phys. Rev. Lett. **102**, 226401 (2009).
- ⁴⁰ J. Sun, A. Ruzsinszky, and J. P. Perdew, Phys. Rev. Lett. **115**, 036402 (2015).
- ⁴¹ J. Sun, R. C. Remsing, Y. Zhang, Z. Sun, A. Ruzsinszky, H. Peng, Z. Yang, A. Paul, U. Waghmare, X. Wu, M. L. Klein, and J. P. Perdew, Nat. Chem. **8**, 831 (2016).
- ⁴² Y. Zhang, D. A. Kitchev, J. Yang, T. Chen, S. T. Dacek, R. A. Samiento-Perez, M. A. L. Marques, H. Peng, G. Ceder, J. P. Perdew, and J. Sun, npj Comput. Mater. **4**, 9 (2018).
- ⁴³ E. B. Isaacs and C. Wolverton, Phys. Rev. Mater. **2**, 063801 (2018).
- ⁴⁴ F. Tran, J. Stelzl, P. Blaha. J. Chem. Phys. **144**, 204120 (2016).
- ⁴⁵ V. Sokolovskiy, D. Baigutlin, O. Miroshkina, V. Buchelnikov, Metals. **13**, 728 (2023).
- ⁴⁶ C. Lane, J. W. Furness, I. G. Buda, Y. Zhang, R. S. Markiewicz, B. Barbiellini, J. Sun, and A. Bansil, Phys. Rev. B **98**, 125140 (2018).
- ⁴⁷ Y. Fu and D. Singh, Phys. Rev. B **100**, 045126 (2019).
- ⁴⁸ J. P. Perdew, A. Ruzsinszky, J. Sun, N. K. Nepal, and A. D. Kaplan, P. N. A. S. **118**, e20178501118 (2021).
- ⁴⁹ A. P. Bartok, and J. R. Yates, J. Chem. Phys. **150**, 161101 (2019).
- ⁵⁰ J. W. Furness, A. D. Kaplan, J. Ning, J. P. Perdew, and J. Sun, J. Phys. Chem. Lett. **11**, 8208 (2020).
- ⁵¹ A. D. J. Becke, Chem. Phys. **98**, 1372 (1993).
- ⁵² A. D. J. Becke, Chem. Phys. **98**, 5648 (1993).
- ⁵³ P. J. Stephens, F. J. Devlin, C. F. Chabalowski, and M. J. Frisch, J. Phys. Chem. **98**, 11623 (1994)
- ⁵⁴ C. Adamo and V. Barone, J. Chem. Phys. **110**, 6158 (1999).
- ⁵⁵ J. P. Perdew, K. Burke, and M. Ernzerhof, Phys. Rev. Lett. **77**, 3865 (1996); Phys. Rev. Lett. **78**, 1396(E) (1997).
- ⁵⁶ J. P. Perdew, M. Ernzerhof, and K. Burke, J. Chem. Phys. **105**, 9982 (1996).
- ⁵⁷ J. Heyd, G. E. Scuseria, and M. Ernzerhof J. Chem. Phys. **118**, 8207 (2003).
- ⁵⁸ J. Heyd, G. E. Scuseria, and M. Ernzerhof J. Chem. Phys. **124**, 219906 (2006).
- ⁵⁹ D. Bohm and D. Pines. Phys. Rev. **92**, 609, (1953).
X. Ren, P. Rinke, C. Joas, and M. Scheffler. J. Mater. Sci., **47**, 7447, (2012).
- ⁶⁰ X. Ren, P. Rinke, C. Joas, and M. Scheffler. J. Mater. Sci., **47**, 7447, (2012).
- ⁶¹ A. V. Krugau, O. A. Vydrov, A. F. Izmaylov, and G. E. Scuseria, J. Chem. Phys. **125**, 224106 (2006).
- ⁶² P. E. Blöchl, C. F. J. Walther, and T. Pruschke, Phys. Rev. B **84**, 205101 (2011).
- ⁶³ V. L. Campo and M. Cococcioni, J. Phys. Condens. Matter **22**, 055602 (2010).
- ⁶⁴ V. I. Anisimov, J. Zaanen, and O. K. Andersen, Phys. Rev. B **44**, 943 (1991).
- ⁶⁵ A. I. Liechtenstein, V. I. Anisimov, and J. Zaanen, Phys. Rev. B **52**, R5467 (1995).
- ⁶⁶ S. Dudarev, G. Botton, S. Savrasov, C. Humphreys, and A. Sutton, Phys. Rev. B. **57**, 1505 (1998).
- ⁶⁷ I. Timrov, F. Aquilante, M. Cococcioni and N. Marzari Phys. Rev. X Energy **1**, 033003 (2022).
- ⁶⁸ O. Gunnarsson, O. Andersen, O. Jepsen, and J. Zaanen, Phys. Rev. B **39**, 1708 (1989).
- ⁶⁹ M. Hybertsen, M. Schlüter, and N. Christensen, Phys. Rev. B **39**, 9028 (1989).
- ⁷⁰ O. Gunnarsson, Phys. Rev. B **41**, 514 (1990).
- ⁷¹ M. Springer and F. Aryasetiawan, Phys. Rev. B **57**, 4364 (1998).
- ⁷² T. Kotani, J. Phys.: Condens. Matter **12**, 2413 (2000).
- ⁷³ F. Aryasetiawan, K. Karlsson, O. Jepsen, and U. Schönberger, Phys. Rev. B **74**, 125106 (2006).
- ⁷⁴ I. Timrov, N. Marzari, and M. Cococcioni, Phys. Rev. B **98**, 085127 (2018).
- ⁷⁵ I. Timrov, N. Marzari, and M. Cococcioni, Phys. Rev. B **103**, 045141 (2021).
- ⁷⁶ H. Kulik and N. Marzari, J. Chem. Phys. **129**, 134314 (2008).
- ⁷⁷ P. O. Löwdin, J. Chem. Phys. **18**, 365 (1950).
- ⁷⁸ Y. C. Wang, Z. H. Chen, and H. Jiang, J. Chem. Phys. **144**, 144106 (2016).
- ⁷⁹ J. Perdew, A. Ruzsinszky, G. Csonka, O. Vydrov, G. Scuseria, L. Constantin, X. Zhou, and K. Burke, Phys. Rev. Lett. **100**, 136406 (2008).
- ⁸⁰ V. I. Anisimov, I. V. Solovyev, M. A. Korotin, M. T. Czyżyk and G. A. Sawatzky, Phys. Rev. B **48**, 16929 (1993).
- ⁸¹ M. T. Czyżyk and G. A. Sawatzky, Phys. Rev. B **49**, 14211 (1994).
- ⁸² I. V. Solovyev, P. H. Dederichs, and V. I. Anisimov, Phys. Rev. B **50**, 16861 (1994).
- ⁸³ P. Giannozzi *et al.*, J. Phys.: Condens. Matter. **21**, 395502 (2009).
- ⁸⁴ P. Giannozzi *et al.*, J. Phys.: Condens. Matter **29**, 465901 (2017).
- ⁸⁵ P. Giannozzi *et al.*, J. Chem. Phys. **152**, 154105 (2020).
- ⁸⁶ P. E. Blöchl, Phys. Rev. B **50**, 17953 (1994).
- ⁸⁷ E. Kucukbenli, M. Monni, B. Adetunji, X. Ge, G. Adebayo, N. Marzari, S. de Gironcoli, and A. Dal Corso, arXiv:1404.3015 (2014).
- ⁸⁸ M. van Setten, M. Giantomassi, E. Bousquet, M. Verstraete, D. Hamann, X. Gonze, and G. M. Rignanese, Comput. Phys. Commun. **226**, 39 (2018).
- ⁸⁹ I. Timrov, N. Marzari, and M. Cococcioni, Comput. Phys. Commun. **279**, 108455 (2022).
- ⁹⁰ I. Mayer, Int. J. Quant. Chem. **90**, 63 (2002).
- ⁹¹ H. J. Monkhorst and J. D. Pack, Phys. Rev. B **13**, 5188 (1976).
- ⁹² P. E. Blöchl, O. Jepsen, and O. K. Andersen, Phys. Rev. B **49**, 16223 (1994).
- ⁹³ N. Marzari, D. Vanderbilt, A. De Vita, and M. Payne,

- Phys. Rev. Lett. **82**, 3296 (1999).
- ⁹⁴ <http://www.cppaw.org>
- ⁹⁵ R. Car and M. Parrinello, Phys. Rev. Lett. **55**, 2471 (1985).
- ⁹⁶ N. D. Mermin, Phys. Rev. **137**, A1441 (1965).
- ⁹⁷ M. Sotoudeh, S. Rajpurohit, P. Blöchl, D. Mierwaldt, J. Norpoth, V. Roddatis, S. Mildner, B. Kressdorf, B. Iffland, and C. Jooss, Phys. Rev. B **95**, 235150 (2017).
- ⁹⁸ A. Houari, and F. Benissad Adv. Theory. Simul. **2** 1900111 (2019).
- ⁹⁹ M. Eckhoff, P. Blöchl, and J. Behler, Phys. Rev. B **101**, 205113 (2020).
- ¹⁰⁰ F. Benissad, and A. Houari, Phys. Status. Solidi. B 2000241 (2020).
- ¹⁰¹ F. Birch, Phys. Rev. **71**, 809 (1947).
- ¹⁰² F. Tran, P. Blaha, K. Schwarz, and P. Novak, Phys. Rev. B **74**, 155108 (2006).
- ¹⁰³ P. Seth, P. Hansmann, A. van Roekeghem, L. Vaugier, and S. Biermann, Phys. Rev. Lett. **119**, 056401 (2017).
- ¹⁰⁴ S. Mandal, K. Haule, K. M. Rabe, and D. Vanderbilt npj Computational Materials **115** 11 (2019).
- ¹⁰⁵ H. M. Hong, Y. J. Kang, J. Kang, E. C. Lee, Y. H. Kim, and K. J. Chang, Phys. Rev. B **72**, 144408 (2005).